Iranian Journal of Geophysics, Vol 18 No 6, 2025, Page 79 – 94 (Research Article)
DOI: 10.30499/ijg.2024.416448.1539

Application of the ground penetrating radar for detecting the subsurface cavities-a case study from the Kariz galleries

Sajjad Ghanbari[1*], Aladin Ebrahimi[2], Mohammad Kazem Hafizi[3], Maksim Bano[4] and Nasrin Faramarzi[5]

[1] *Assistant Professor, Physics Department, Faculty of Sciences, Razi university, Kermanshah, Iran*
[2] *Ph.D., Department of Computer Science and Information Technology, La Trobe University, Melbourne, Australia*
[3] *Professor, Institute of Geophysics, University of Tehran, Iran*
[4] *Associate Professor, Ecole et observatoire Université de Strasbourg, Strasbourg, France*
[5] *M.Sc. Graduate, Razi university, Kermanshah, Iran*

(Received: 15 September 2023, Accepted: 19 April 2024)

Abstract

In general, a quantitative analysis of ground-penetrating radar (GPR) data provides insights into the depth of sources and underlying geological features. This study compares the depth information obtained from GPR waves using diverse approaches to detect underground cavities. The processing techniques, including conventional processing (Kirchhoff migration), time reversal (TR) imaging, and the application of continuous wavelet transform (CWT) in TR imaging, known as compensated time reversal (CTR), are evaluated in comparison to commercial software. The predicted depths from TR and CTR align closely with drilling results, while traditional processing and Kirchhoff migration occasionally fall short in identifying distinct targets. Subsequently, we focused on typical subsurface cavities in urban areas, known as Kariz (ancient aqueducts), situated at three locations in Kashan, Iran, encompassing two active (water-carrying) and one dried Kariz. The TR and CTR results demonstrate the applicability of both techniques for additional applications, showcasing their effectiveness in estimating the depth of Kariz galleries using GPR signals.

Keywords: Kariz, ancient aqueduct, GPR, time reversal imaging, CTR

[*]Corresponding author: sajjad.ghanbari@alumni.ut.ac.ir

1 Introduction

In contemporary times, geophysical methods have proven instrumental in identifying a plethora of abandoned mine tunnels and underground cavities. These techniques play a crucial role in monitoring sub-surface features and addressing environmental concerns, with ground-penetrating radar (GPR) standing out as one of the quickest and most accessible technologies (Ebrahimi et al., 2012, 2017; Baawain et al., 2018). Ancient aqueducts, such as the widely investigated Kariz, serve as illustrative examples in cavity detection across various regions. The term "Kariz" which holds significance for the Middle East and West Asia, represents a hydraulic system known by diverse names across approximately 35 countries (English, 1968; Golbot, 1979; Moosavi, 2006; Mahmoudi et al., 2017; Ebrahimi et al., 2021). Fig. 1 presents a conceptual model of a Kariz system extensively employed in existing networks. This network comprises vertical monitoring wells or shafts intersecting a lengthy horizontal gallery, extending from an aquifer to the outlet. Kariz systems contribute to enhancing water accessibility for agricultural and urban purposes, particularly in arid regions. Historical records suggest that the Persians pioneered Kariz technology in ancient Iran during the first millennium BC, with its gradually spreading influence westward and eastward (English, 1968; Golbot, 1979; Miller, et al., 2009).

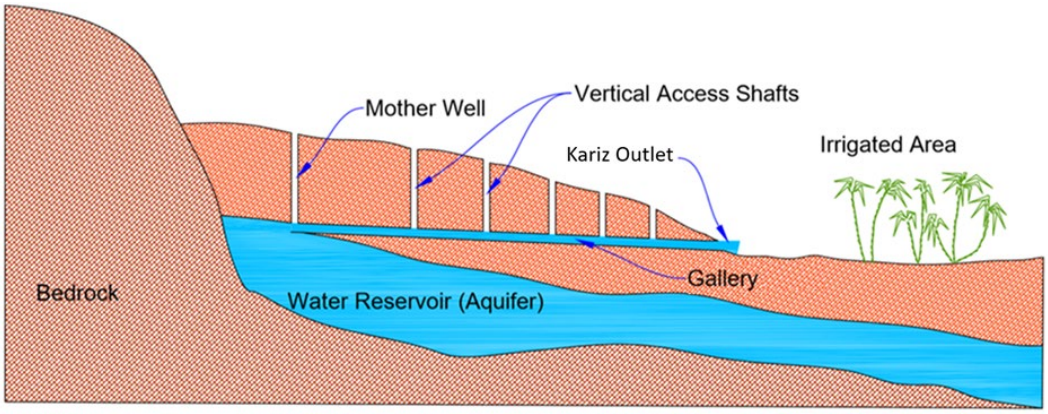

Figure 1. A typical Kariz network structure (based on Ebrahimi et al., 2021).

In Kariz investigations, both qualitative and quantitative techniques, such as geoengineering, hydrology, geographic information systems (GIS), and geophysics play pivotal roles (Benjelloun et al., 2018; Ebrahimi et al., 2021). Geophysical approaches are renowned for their speed and reliability in data acquisition, particularly in uncovering hidden galleries (Cardarelli et al., 2010; Ebrahimi et al., 2019). Techniques like gravity and electrical resistivity prove effective in detecting Kariz channels and exploring subsurface galleries (Hajian et al., 2011; Ebrahimi et al., 2019).

Geoscientific investigations may encounter constraints from a geological standpoint, particularly in cases where the water source is from a relatively shallow unconfined aquifer, and the surrounding material comprises clay, high alluvium, or colluvial deposits. Electromagnetic (EM)-based techniques in such scenarios experience greater damping phenomena, leading to decreased resolution (Cardarelli et al., 2006; Brinon and Kessouri, 2009). The application of an integrated method or multi-dimensional

processing can help overcome or, at the very least, restrict such constraints. Ground-penetrating radar (GPR) complements these methods by assisting in pinpointing the location, approximate diameter, and soil saturation coefficient of the surrounding medium of the galleries (Hajian et al., 2011; Ghanbari and Hafizi, 2013, 2016; Ebrahimi et al., 2017; Ebrahimi et al., 2019; Dawrea et al., 2021; Kotb et al., 2021; Tao et al., 2022).

GPR, a commonly employed technique in near-surface engineering projects (Ortega et al., 2010; Ebrahimi et al., 2012; Ghanbari and Hafizi, 2013; Leucci et al., 2016; Blanco et al., 2021), has been the subject of numerous case studies focusing on dry or active Kariz networks, considering both field and technological concerns (Rousset et al., 2009; Tosti and Slob, 2015; Glaser et al., 2021). The choice of antenna, including the consideration of lower center frequencies for increased depth and potential trade-offs in resolution, is critical and demands careful assessment by engineers before conducting surveys (De Benedetto et al., 2015; Ali et al., 2021; Ganther, 2021; Thomas and Roy, 2021).

GPR signal processing requires meticulous attention due to factors like ground clutter, ground losses, and geological inhomogeneity contributing to unclear target responses. Several GPR processing techniques, including traditional settings like bandpass filters, background removal, gain functions, and migration techniques can enhance the resolution of radargrams (Di Prinzio et al., 2010; Mirhosseini et al., 2015; Santos and Teixeira, 2017; Ebrahimi et al., 2017; Dos Santos et al., 2018; Lau et al., 2021; Zhang et al., 2021; Liu et al., 2021). Continuous improvements in processes, moving beyond conventional GPR signal processing, contribute to enhanced resolution and precision in GPR sections through the application of sophisticated techniques.

Engineers commonly employ conventional processing for industrial applications. Commercial software provides straightforward techniques for reducing unwanted characteristics or noise, including bandpass filtering, moving averages, and gain functions (Park and Kim, 2020).

Time Reversal (TR) imaging (Baysal et al., 1983; Prada et al., 1991) is another effective technique that focuses on received signals reversed based on time. The location of the original source is enlarged in this direction since the wave equation in TR forms is a backpropagating wave (Lerosey et al., 2005). Because wave equations in lossless media are invariant, the TR technique can spatiotemporally refocus back-propagated signals in a particular ultrawideband imaging scenario (Abduljabbar et al., 2017). For a cavity or a Kariz gallery bordered by clay and silty material, as a secondary source, the TR principle can be utilized to determine its uncertain position (Carminati et al., 2007; Gu et al., 2015; Panagiotopoulos and Stavroulakis, 2021). Several case studies have investigated the application of TR to GPR signal processing, yielding encouraging results (Santos and Teixeira, 2017; Dos Santos et al., 2018; Bicudo et al., 2020).

In a lossy medium, such as that around a Kariz gallery, the presence of dispersion and loss breaks the invariance of wave equations, resulting in the attenuation of signals produced after TR application. In this scenario, compensating for such effects requires the use of an inverse filter. A method for microwave propagation using the Continuous Wavelet Transform (CWT) approach, which incorporates both time and frequency variations, was proposed by Ammar et al. (2017).

CWT employed here (Poisson et al., 1999) is a discrete transform of a signal that allows for noise reduction, data compression, and peak detection, all of which are useful in GPR signal processing (Gutierrez et al., 2019; Kumar et al., 2020). As a similar approach, a comparative study based on CTR and TR imaging has been researched for GPR signals (Ghanbari et al., 2024). The significance of CTR has been explored in the literature (Yavuz and Teixeira, 2006; Yavuz et al., 2014; Abduljabbar et al., 2017; Ghanbari et al., 2022), yet it takes longer to finish a processing task than TR (see Appendix A).

In this research, our focus centers on the exploration of four distinct processing algorithms applied to GPR radargrams acquired within Kariz networks spanning three distinct locations in Kashan, Iran. While conventional processing stands as a widely employed methodology in near-surface applications, including commercial software, our exploration delves into the nuanced benefits and drawbacks associated with diverse migration methods such as Time Reversal and its compensated type.

Our distinctive contribution lies in the meticulous comparison of results stemming from various antennas, affording us a pragmatic understanding of the most efficient frequency within the 250 to 500 MHz range. By doing so, we aim to provide a novel perspective on the optimization of GPR techniques for subsurface investigations, elucidating both the strengths and limitations of established and emerging methodologies.

2 Methodology

The GPR process is fundamentally grounded in the theoretical framework of electromagnetic wave reflection and diffraction phenomena from subsurface layers and anomalies. In this process, a transmitter emits a signal into the earth, and upon encountering a subsurface anomaly, the signal undergoes reflection or diffraction and ultimately, is redirected toward the receiver. This methodology is applicable to the analysis of both active Kariz networks (those carrying water downstream) and dry Kariz networks (Jol, 2008; Dawrea et al., 2021).

To provide a visual representation of this process, Fig. 2 illustrates a generalized view of EM waves propagating through a material within the Kariz gallery, with the GPR profile oriented perpendicular to the wave propagation. Notably, the darker hyperbolic event in Fig. 2b signifies an enhanced contrast in electromagnetic properties (reflected coefficient) compared to Fig. 2a. This distinction serves as a key indicator of subsurface anomalies, emphasizing the sensitivity of GPR in detecting variations in EM properties within Kariz networks. The amplitudes and reflection coefficients of electromagnetic (EM) waves in the boundaries of diverse media, including Kariz galleries, indicate that cavities containing water exhibit higher resolution than their dry counterparts (Neal, 2004).

To expound on the following processing methods, it is essential to grasp the underlying principles of the Time Reversal (TR) method. TR involves a sequence of four steps: (1) transceivers emit a pulse signal; (2) this emitted signal traverses the predominant medium and subsequently encounters reflections from various targets; (3) transceivers collect the reflected signals; (4) the received signals undergo a reversal in time and are reintroduced into the medium. Back-propagation can be achieved either physically, using transceivers, or synthetically, employing a forward simulation engine like the finite-difference time-domain (FDTD) method (Santos and Texeira, 2017).

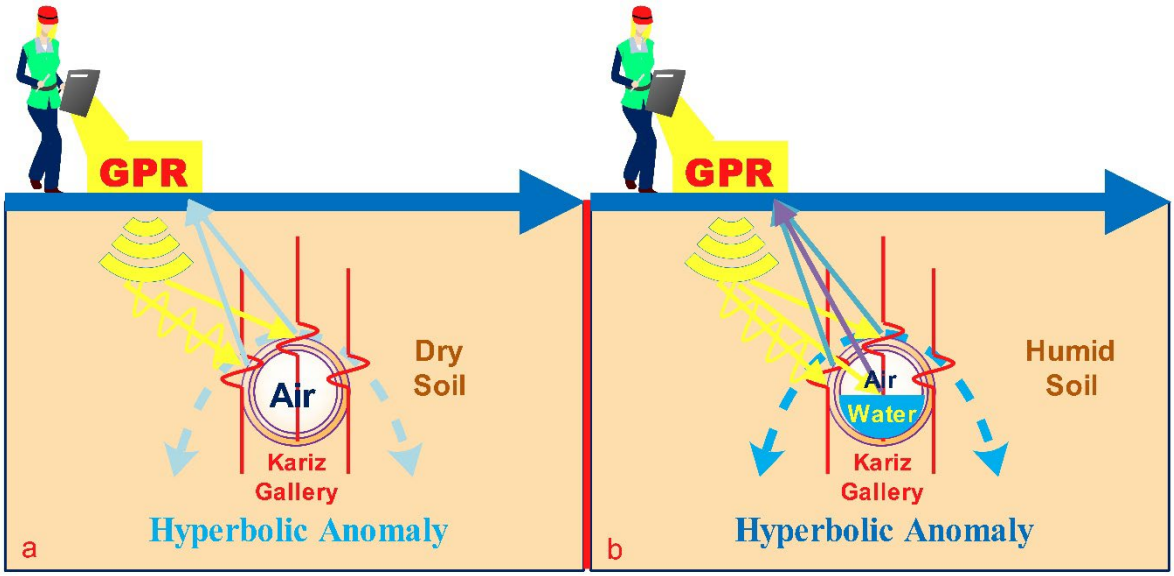

Figure 2. Schematic representation of the GPR approach applied in the field for (a) a dried and (b) an active Kariz. The arrows indicate the direction of a typical traversal, while the darker circular arrow atop the gallery denotes a sharper and clearer response of electromagnetic (EM) waves when encountering an active Kariz, as illustrated in part (b), in contrast to a dried one.

In the presence of a dispersive and lossy medium, acting as a low-pass filter, the invariance of wave equations is disrupted, leading to signal attenuation. Consequently, inverse filters become necessary for compensation. During forward signal propagation, the real part of the dielectric permittivity (ε) of the medium induces a phase shift in the traveling waves. The TR concept dictates that the back-propagated signal is phase-conjugated coherently across all bandwidths, inherently correcting the phase shift (Yavuz and Texeira, 2009; Abduljabbar et al., 2017; Ghanbari et al., 2022). However, the imaginary part of the dielectric permittivity introduces inevitable signal attenuation, contingent on signal frequency and the duration of signal propagation in a dispersive medium.

To address the challenge of attenuation, Abduljabbar et al. (2017) proposed a method utilizing the CWT technique, which incorporates both time and frequency variations for microwave propagation.

3 Descriptions and data acquisition

GPR data were collected at three distinct sites in Kashan, Iran, where the typical depth of Kariz galleries ranged from 1 to 2 meters near the Kariz outlet. The main objective at location 1 was to precisely locate an active underground Kariz using a 500 MHz central frequency antenna. In contrast, locations 2 and 3, employing a 250 MHz antenna, were dedicated to identifying galleries of both an active and a dried Kariz.

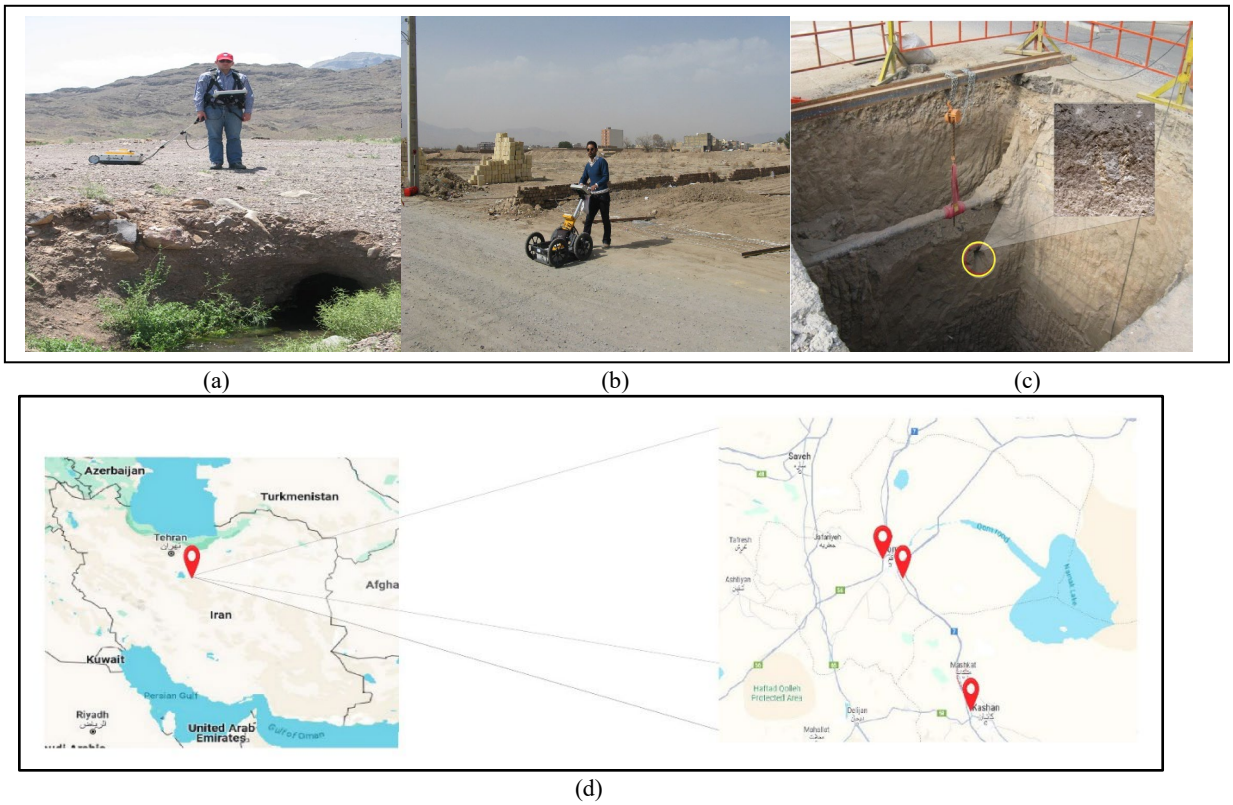

(a) (b) (c)

(d)

Figure 3. (a) Kariz outlet at location 1 showcasing the GPR setup featuring the 500 MHz central frequency antenna. (b) Data acquisition at location 3. (c) Drilling trench revealing the identified gallery at location 3. The yellow circle highlights the gallery, which has become dry and filled due to drilling. It displays traces of prior water flow over time. (d) Geographical locations of the investigated sites.

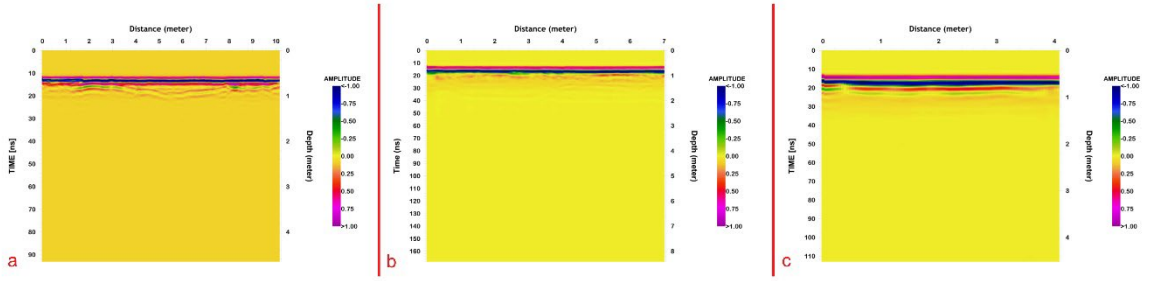

(a) (b) (c)

Figure 4. Raw radargrams related to (a) location 1, (b) location 2, (c) location 3.

Fieldwork samples from the survey at location 2 are depicted in Fig. 3a, while Figs. 3b and 3c showcase a dried Kariz after drilling in location 2 and the positioning of Kariz 3, respectively. Furthermore, Fig. 4 presents the radargrams acquired at each location.

4 Data processing and interpretation

An essential step in GPR data processing, known as velocity analysis, focuses on determining the electromagnetic (EM) wave velocity within a specific medium, particularly one divided into layers. The outcome significantly influences subsequent stacking and migration procedures. The GPR wave velocity (V) is determined by the relative dielectric permittivity (ε_r) and the EM wave velocity in a vacuum (C = 0.3 m/ns) (Ulaby, 2010):

$$V = \frac{c}{\sqrt{\varepsilon_r}} \quad (1)$$

According to laboratory measurements, the relative permeability values for active and dried aqueducts were determined as 9

and 14, respectively. Consequently, the velocity for an active Kariz medium is assessed as V = 0.1 m/ns, while for a dried Kariz, it is determined as V = 0.08 m/ns.

All GPR radargrams underwent pre-processing using the following procedures (Fig. 4): time-zero shifts; low-frequency elimination or DC filtering (dewow); muting traces with improper amplitudes. The software processes in this study were conducted using Reflex Project and MATLAB software, with the utilized GPR device being a MALA.

After completing the outlined processes, the data is now prepared for advanced processing. To examine how the anticipated features manifest on the sections, four different procedures were applied separately to each pre-processed radargram (locations 1 and 2). Initially, the data underwent standard processing, involving band-pass filtering, average removal, and a gain function. Band-pass filtering was tailored based on the frequency range of the antenna, with lower and upper bounds of half its center frequency and half its frequency, respectively. Alternatively, it could have lower and upper bounds of twice its center frequency and four times its center frequency. Subsequently, to provide a more precise depiction of the below-ground layers, Kirchhoff migration was tested.

The third processing technique involved the application of a TR imaging technique, which helps mitigate signal losses caused by humidity and conductive rocks in the gallery. As the fourth approach, CTR was applied to the sections. CTR was found to be an effective method for enhancing the resolution of attenuated signals caused by a TR filter by incorporating a CWT into it (Abduljabbar et al., 2017). Figs. 5, 6, and 7 depict the application of the four processing methods described above to GPR data acquired at locations 1 and 2.

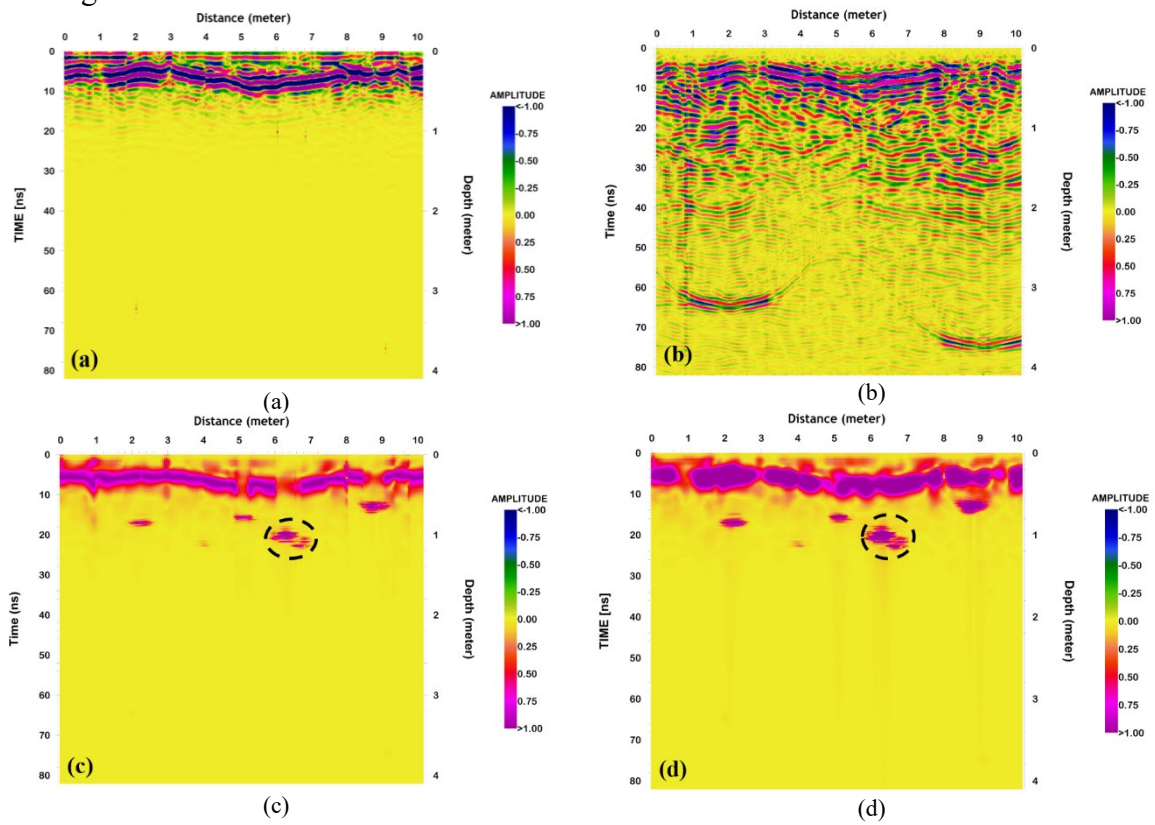

Figure 5. Radargrams from location 1 processed using (a) traditional processing (b) Kirchhoff migration (c) TR imaging (d) CTR. The dashed circles denote localized concentration points within the domain, identified by the Kariz gallery.

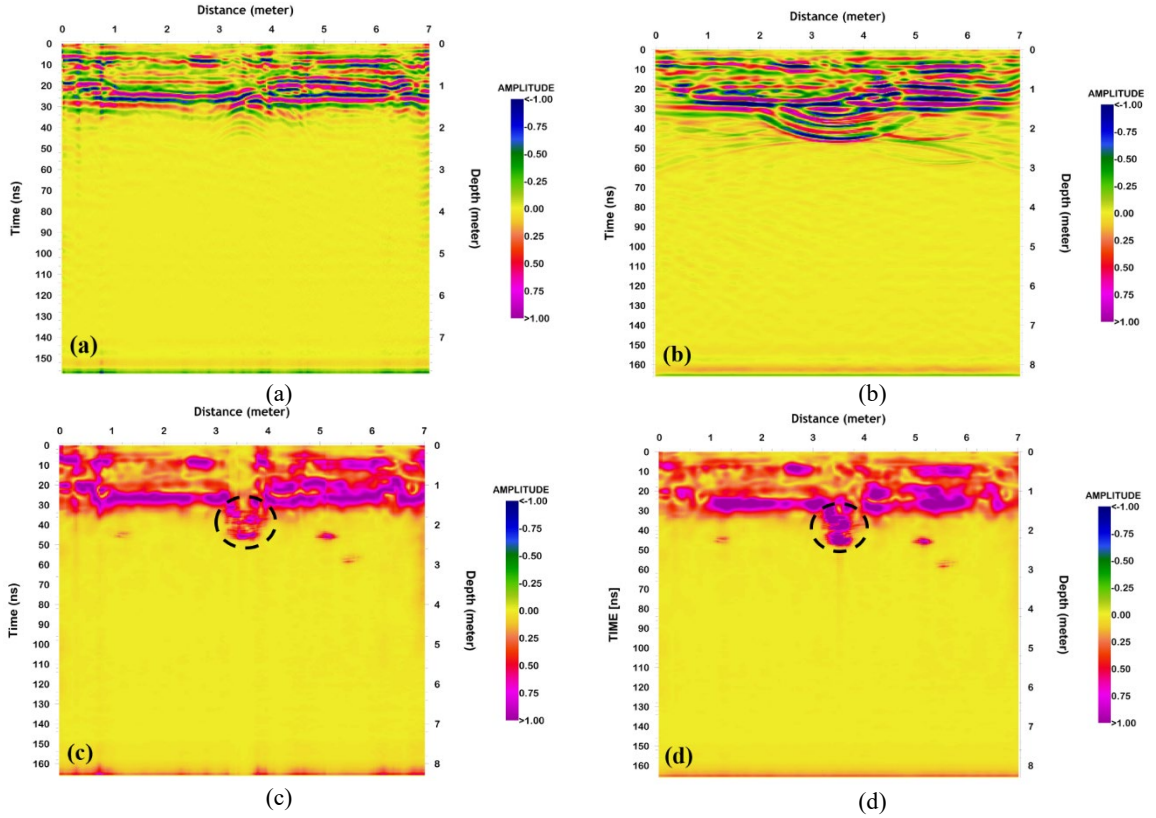

Figure 6. Radargrams from location 2 processed using (a) traditional processing (b) Kirchhoff migration (c) TR imaging (d) CTR. The dashed circle highlights localized concentration regions within the domain, associated with the presence of a Kariz gallery.

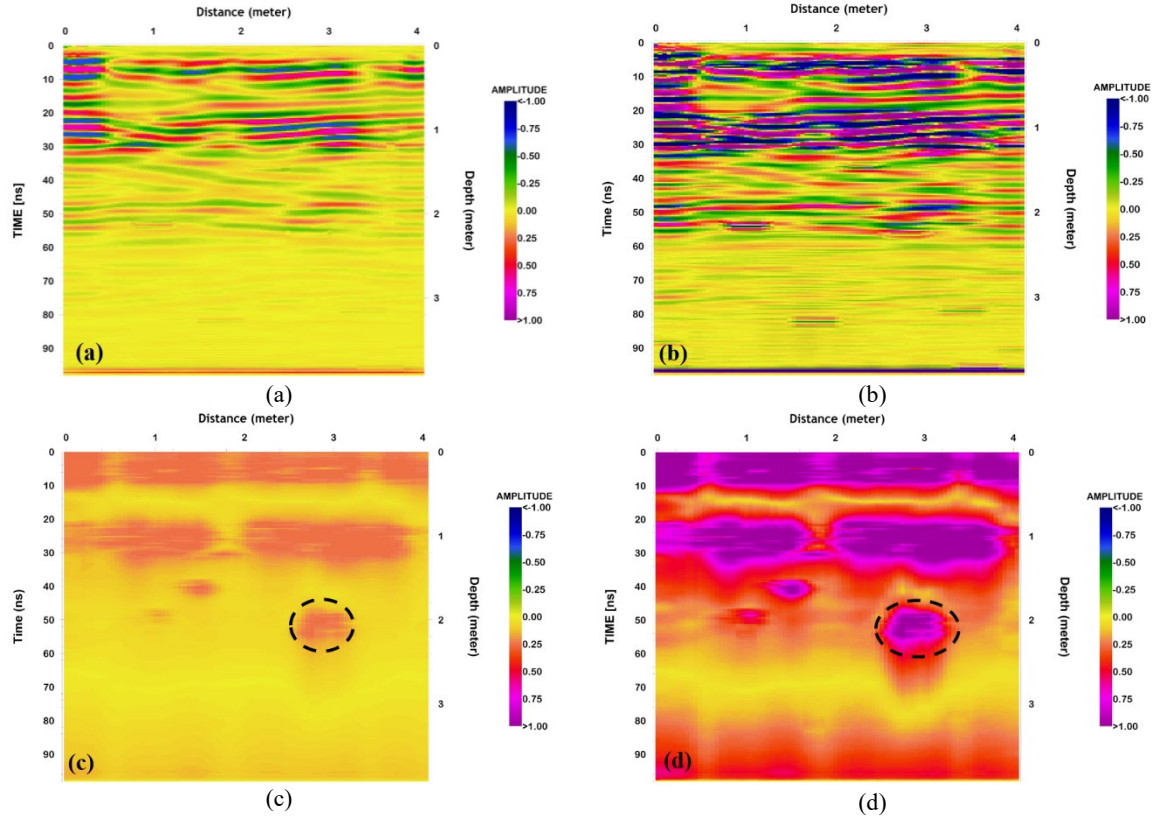

Figure 7. Radargrams from location 3 processed using (a) traditional processing (b) Kirchhoff migration (c) TR imaging (d) CTR. The dashed circles highlight the localized focusing zones within the domain, constituting the interpreted anomaly of a Kariz gallery.

The results from location 1 (Fig. 5) provide a comprehensive depiction of near-surface layers through all processing approaches. However, traditional processing (Fig. 5a) fell short in presenting attributes corresponding to the presence of the gallery. Kirchhoff migration (Fig. 5b) successfully migrated the relocated hyperbolic events. TR imaging (Fig. 5c) demonstrated the upper section of the gallery marked by a dashed-circle, highlighting localized focusing zones, along with a clear representation of near-surface layers, akin to traditional processing. In contrast, CTR (Fig. 5d) identified an intense area around 6-7 m horizontal offset and an approximate depth of 1 m, indicated by a circle, representing the upper part of the gallery and near-surface layers up to 0.6 m depth. It's noteworthy that high-energy locations in other sections may suggest the presence of rocks or other anomalies.

For location 2, subjected to the same four processing techniques (Fig. 6), traditional processing (Fig. 6a) revealed detailed near-surface layers down to 1 m and a hyperbolic peak at a horizontal offset of 3-4 m and an approximate depth of 1.5 m, represented by a dashed-circle. Kirchhoff migration (Fig. 6b) helped identify larger amplitudes in the location of the gallery at a similar depth, but additional reverberations rendered the radargram noisy. TR imaging (Fig. 6c) exhibited clear near-surface layers, emphasizing internal water and the gallery with highly concentrated amplitudes at depths around 1.5 m, highlighted by a circle. The CTR approach (Fig. 6d) yielded outcomes similar to TR but with slightly higher resolution.

In interpreting radargrams of the dried Kariz at location 3 (Fig. 7), TR (Fig. 7c) and CTR (Fig. 7d) methods revealed the depth of the gallery (2 m) and the strata close to the surface (up to 1.5 m in depth). Kirchhoff migration (Fig. 7b) and standard processing (Fig. 7a) displayed the overburden layers. Detecting a buried dried Kariz is challenging due to the contrast between water in the gallery and the surrounding medium. It causes hyperbolic reactions in the radargrams and enhances the readability of the GPR section. Table 1 summarizes the findings from all processing methods, with ε_r values obtained through laboratory experimental measurements.

Table 1. A comparison of estimated depths (in meters) to the top of the Kariz galleries determined by conventional, TR, Kirchhoff migration, and CTR processings, along with summaries of the processing methods.

frequency	status	traverse length	actual depth, by drilling	mean value of εr	mean value of velocity (m/ns)	estimated depth by **Conventional** method	estimated depth by **TR**	estimated depth by **Kirchhoff migration**	estimated depth by **CTR**
500 MHz, location 1	active	~10 m	1 m	9	0.1	-	~1 m	-	~1 m
250 MHz, location 2	active	~7 m	1.5 m	9	0.1	~1.5 m	~1.5 m	~1.5 m	~1.5 m
250 MHz, location 3	dried	~4 m	2 m	14	0.08	-	~2 m	-	~2 m

In practice, it is evident that the application of a 250 MHz antenna takes precedence over a 500 MHz antenna for both dried and active Karizes, especially in galleries located at depths of 1 to 2 meters. This conclusion is drawn from the obtained results, considering a field with geological characteristics similar to the current case studies, characterized by a medium composed of silt, clay, or porous rocks. Consequently, TR and CTR techniques are strongly recommended for

processing GPR data from dry Kariz networks or data containing a significant amount of geological noise, even though standard processing remains adequate for an active Kariz.

To quantitatively compare the outcomes of CTR processing against traditional methods, the Signal to Noise Ratio (SNR) is employed. The SNR is theoretically calculated by dividing the measured source value by the noise. In this context, noise is determined as the value of the image at the accurate source site over the noise, being the greatest value of the picture outside of a zone around the genuine source position (Petromichelakis et al., 2018). Therefore, the SNR formula can be expressed as (Li et al., 2019):

$$\mathrm{SNR}\sim 20\log\frac{A_s}{A_n} \quad (2)$$

where A_s and A_n are the amplitude of the target reflection peak and the amplitude of the noise peak, respectively. Table 2 displays the computed SNR for the relevant GPR signals.

Table 2. Signal to Noise Ratio (SNR) analysis of traverses (locations 1, 2, and 3) utilizing Kirchhoff Migration (KM), Time Reversal (TR), Compensated Time Reversal (CTR), and Conventional Processing (CP).

Site no.	SNR values				Quality increase ratio based on SNR radargram processed by conventional processing (CP)		
	CP	CP+KM	TR	CTR	CP+KM	TR	CTR
location 1	8	9	10	11	1.12	1.25	1.37
location 2	9	10	11	12	1.11	1.22	1.33
location 3	7	7	9	10	1	1.28	1.42

5 Conclusion

This study employed four distinct processing methodologies and utilized antennas with central frequencies of 250 MHz and 500 MHz to explore the efficacy of GPR signal processing in detecting hidden galleries, specifically in two dried Kariz and one active Kariz. Traditional processing and Kirchhoff migration exhibited limitations, particularly in scenarios involving dried Kariz or data acquisition with a 500 MHz central frequency antenna. In contrast, time reversal processing (TR) and TR coupled with attenuation compensation (CTR) proved instrumental in enhancing radargram resolution. Both TR and CTR approaches demonstrated proficiency in distinguishing abnormalities within a lossy medium. While TR imaging accurately identified the gallery position, the CTR method offered superior characterization of subsurface gallery reflectors, albeit with a time-intensive processing duration. The findings were substantiated through seismic profiling and borehole drilling, underscoring the reliability of the geophysical operations conducted in this investigation.

Conflict of Interest

No conflict of interests.

Acknowledgements

The authors of the research would like to convey their profound gratitude to the Institute of Geophysics, the University of Tehran for funding this research. Also, thanks to all of the field men who helped with the work, as well as the ZAP Consulting Engineers Company.

References

Abduljabbar, A. M., Yavuz, M. E., Costen, F., Himeno, R., and Yokota, H., 2017, Continuous wavelet transform-based frequency dispersion compensation method for electromagnetic time-reversal imaging: IEEE Transactions on Antennas and Propagation, **65**(3), 1321-1329.

Ali, Z., Abid, G., Kumar, C., Memon, V., and Siddiqui, A., 2021, Impact of ultra-wideband antenna application on underground object detection: International Journal of Advanced Trends in Computer Science and Engineeting, **10**(3), 2441-2446.

Annan, A. P., 2005, GPR Methods for Hydrogeological Studies, in Rubin, Y., Hubbard, S. S., eds., Hydrogeophysics, Water Science and Technology Library, **50**: Springer, Dordrecht, https://doi.org/10.1007/1-4020-3102-5_7.

Baawain, M. S., Al-Futaisi, A. M., Ebrahimi, A., and Omidvarborna, H., 2018, Characterizing leachate contamination in a landfill site using Time Domain Electromagnetic (TDEM) imaging: Journal of Applied Geophysics, **151**, 73-81.

Baysal, E., Kosloff, D. D., and Sherwood, J. W., 1983, Reverse time migration: Geophysics, **48**(11), 1514-1524.

Benjelloun, Y., de Sigoyer, J., Dessales, H., Garambois, S., and Şahin, M., 2018, Construction history of the aqueduct of Nicaea (Iznik, NW Turkey) and its on-fault deformation viewed from archaeological and geophysical investigations: Journal of Archaeological Science: Reports, **21**, 389-400.

Bicudo, T. C., dos Santos, V. R. N., Porsani, J. L., and Teixeira, F. L., 2020, 3D GPR characterization of buried metallic and plastic tanks using time-reversal processing technique: 18th International Conference on Ground Penetrating Radar, Society of Exploration Geophysicists, 128-131.

Blanco, D., Alessandri, L., Baiocchi, V., et al., 2021, A new branch of the Anio Novus Aqueduct (Rome, Italy) revealed by archaeology and geophysics: ISPRS Annals of the Photogrammetry, Remote Sensing and Spatial Information Sciences, **8**, 49-56.

Braga, I. L. S., and Moraes, F. S., 2013, High-resolution gathers by inverse Q filtering in the wavelet domain: Geophysics, **78**(2), V53-V61.

Brinon, C., and Kessouri, P., 2009, Geophysical prospection of an archaeological site (Grand, France): Characterization of a hydraulic system in a karstic context: ArcheoSciences, Revue d'archéométrie, **33** (suppl.), 39-41.

Cardarelli, E., Cercato, M., Cerreto, A., and Di Filippo, G., 2010, Electrical resistivity and seismic refraction tomography to detect buried cavities: Geophysical Prospecting, **58**(4), 685-695.

Cardarelli, E., Di Filippo, G., and Tuccinardi, E., 2006, Electrical resistivity tomography to detect buried cavities in Rome: a case study: Near Surface Geophysics, **4**(6), 387-392.

Carminati, R., Pierrat, R., De Rosny, J., and Fink, M., 2007, Theory of the time reversal cavity for electromagnetic fields: Optics Letters, **32**(21), 3107-3109.

Dawrea, A., Zytner, R. G., and Donald, J., 2021, Enhanced GPR data interpretation to estimate in situ water saturation in a landfill: Waste Management, **120**, 175-182.

De Benedetto, D., Quarto, R., Castrignanò, A., and Palumbo, D. A., 2015, Impact of data processing and antenna frequency on spatial structure modelling of GPR data: Sensors, **15**(7), 16430-16447.

De Rosny, J., Lerosey, G., and Fink, M., 2010, Theory of electromagnetic time-reversal mirrors: IEEE Transactions on Antennas and Propagation, **58**(10), 3139-3149.

Di Prinzio, M., Bittelli, M., Castellarin, A., and Pisa, P. R., 2010, Application of GPR to the monitoring of river embankments: Journal of Applied Geophysics, **71**(2-3), 53-61.

Dos Santos, V. R. N., Almeida, E. R., Porsani, J. L., Teixeira, F. L., and Soldovieri, F., 2018, A controlled-site comparison of microwave tomography and time-reversal imaging techniques for gpr surveys: Remote Sensing, **10**(2), 214.

Ebrahimi, A., Dehghan, M. J., and Ashtari, A., 2019, Contribution of gravity and Bristow methods for Karez, (aqueduct) detection: Journal of Applied Geophysics, **161**, 37-44.

Ebrahimi, A., Ghanbari, S., and Ashtari, A., 2012, FDTD numerical GPR stratigraphy modeling and processing and a case study with GPR data: Istanbul 2012-International Geophysical Conference and Oil and Gas Exhibition, Society of Exploration Geophysicists and the Chamber of Geophysical Engineers of Turkey, 1-4.

Ebrahimi, A., Gholami, A., and Nabi-Bidhendi, M., 2017, Sparsity-based GPR blind deconvolution and wavelet estimation: The Journal of Indian Geophysical Union, **21**(1), 7-12.

Ebrahimi, A., Mehraban, Y., Omidvarborna, H., Vakilinejad, A., and Al-Sayigh, A. R. S., 2021, Kariz (ancient aqueduct) system: a review on geoengineering and environmental studies: Environmental Earth Sciences, **80**(6), 1-13.

English, P. W., 1968, The origin and spread of qanats in the Old World: Proceedings of the American Philosophical Society, **112**(3), 170-181.

Farge, M., 1992, Wavelet transforms and their applications to turbulence: Annual Review of Fluid Mechanics, **24**(1), 395-458.

Ganther, T., 2021, Measurements and numerical simulations of the effects of inclination and height of a GPR antenna above ground: MSc. Thesis,

Ghanbari, S., and Hafizi M. K., 2013, The effect of antenna central frequency and application of advanced processing in locating buried urban utilities by GPR method: Iranian Journal of Geophysics, **7**(3), 93-106 (in Persian).

Ghanbari, S., and Hafizi M. K., 2016, Application of forward modelling and processing algorithm in Ghanat detection by GPR: Iranian Journal of Geophysics, **10**(2), 67-82 (in Persian).

Ghanbari, S., Hafizi, M. K., Bano, M., Ebrahimi, A., and Hosseinzadeh, N., 2022, An enhanced GPR-based data processing approach for detecting subsurface utilities in urban distribution networks: Journal of Applied Geophysics, **207**, 104831.

Ghanbari, S., Hafizi, M. K., Bano, M., Ebrahimi, A., and Webb, J., 2024, A comparative study of GPR data processing based on Compensated Time-Reversal and Time-Reversal imaging: Bulletin of Geophysics and Oceanograph, **65**(1), 1-16, DOI 10.4430/bgo00434.

Glaser, D. R., Burch, K., Brinkley, D. L., and Reppert, P., 2021, Localization of deep voids through geophysical signatures of secondary dewatering features: Geophysics, **86**(3), WA139-WA152.

Golbot, H., 1979, Les Qanats. Une technique d'acquisition de l'eau. Paris, France: Éditions Mouton, École des hautes études en sciences sociales., Centre de RecherchesHistoriques, Industrie et artisanat, **9**(1).

Gu, B., Li, Z., Ma, X., and Liang, G., 2015, Multi-component elastic reverse time migration based on the P-and S-wave separated velocity–stress equations: Journal of Applied Geophysics, **112**, 62-78.

Gutierrez, S., Vega, F., González, F. A., Baer, C., and Sachs, J., 2019, Application of polarimetric features and support vector machines for classification of improvised explosive devices: IEEE Antennas and Wireless

Propagation Letters, **18**(11), 2282-2286.

Hajian, A., Ardestani, E. V., and Lucas, C., 2011, Depth estimation of gravity anomalies using Hopfield neural networks: Journal of Earth and Space Physics, **37**(2), 1–9.

Jol, H. M. (ed.), 2008, Ground Penetrating Radar: Theory and Applications: Elsevier.

Kotb, A., Basheer, A. A., Nasser, A., and Ramah, M., 2021, Utilizing ERT and GPR to distinguish structures maleficence the constructions in the new administrative capital: Egyptian Earth, **10**(5), 234-243.

Kumar, S., Pal, S. K., and Rani, S., 2020, GPR data interpretation using continuous wavelet transform: a different approach: Current Science (00113891), **118**(7).

Lau, P. K. W., Cheung, B. W. Y., Lai, W. W. L., and Sham, J. F. C., 2021, Characterizing pipe leakage with a combination of GPR wave velocity algorithms: Tunnelling and Underground Space Technology, **109**, 103740.

Lerosey, G., De Rosny, J., Tourin, A., Derode, A., Montaldo, G., and Fink, M., 2005, Time reversal of electromagnetic waves and telecommunication: Radio Science, **40**(6).

Leucci, G., Parise, M., Sammarco, M., and Scardozzi, G., 2016, The use of geophysical prospections to map ancient hydraulic works: the Triglio underground aqueduct (Apulia, Southern Italy): Archaeological Prospection, **23**(3), 195-211.

Li, J., Guo, T., Leung, H., Xu, H., Liu, L., Wang, B., and Liu, Y., 2019, Locating underground pipe using wideband chaotic ground penetrating radar: Sensors, **19**(13), 2913.

Liu, D., Kang, G., Li, et al., 2005, Electromagnetic time-reversal imaging of a target in a cluttered environment: IEEE Transactions on Antennas and Propagation, **53**(9), 3058-3066.

Liu, H., Shi, Z., Li, J., Liu, C., Meng, X., Du, Y., and Chen, J., 2021, Detection of road cavities in urban cities by 3D ground-penetrating radar: Geophysics, **86**(3), WA25-WA33.

Mahmoudi, D., Rezaei, M., and Barmaki, M. D., 2017, Qanat, a technique appropriate for extracting water from hard rock terrains: the case study of Bilvar district, Kurdistan, Iran: International Journal of Hydrology Science and Technology, **7**(2), 188-196.

Miller, F. P., Vandome, A. F., and McBrewster, J., 2009, Aqueduct: Qanat, Roman aqueduct, drought. earthquake engineering, goldfields water supply scheme, irrigation, leat, list of Roman bridges, pipeline transport of accient Rom, Roman engineering: Alphascript Publishing.

Mirhosseini, F., Momeni, M., and Shafiei, E., 2015, Underground cavities investigation using geophysical method, GPR (case study: Kerman city): Current World Environment, **10** (Special Issue), 82.

Moosavi, S. A. A., 2006, Qanat invention puzzle: Proceedings 1st IWA International Symposium Water and Wastewater Technologies in Ancient Civilizations, National Agricultural Research Foundation, Iraklio, 28-30.

Morlet, J., Arens, G., Fourgeau, E., and Glard, D., 1982, Wave propagation and sampling theory—Part I: Complex signal and scattering in multilayered media: Geophysics, **47**(2), 203-221.

Neal, A., 2004, Ground-penetrating radar and its use in sedimentology: principles, problems and progress: Earth-Science Reviews, **66**(3-4), 261-330.

Ortega, A. I., Benito-Calvo, A., Porres, J., Pérez-González, A., and Martín Merino, M. A., 2010, Applying electrical resistivity tomography to the

identification of endokarstic geometries in the Pleistocene sites of the Sierra de Atapuerca (Burgos, Spain): Archaeological Prospection, **17**(4), 233-245.

Panagiotopoulos, C. G., and Stavroulakis, G. E., 2021, A numerical study on computational time reversal for structural health monitoring: Signals, **2**(2), 225-244.

Park, J. J., and Kim, I. D., 2020, Analysis of the under pavement cavity growth rate using multi-channel GPR equipment: Journal of the Society of Disaster Information, **16**(1), 60-69.

Petromichelakis, I., Tsogka, C., and Panagiotopoulos, C. G., 2018, Signal-to-noise ratio analysis for time-reversal based imaging techniques in bounded domains: Wave Motion, **79**, 23-43.

Poisson, O., Rioual, P., and Meunier, M., 1999, New signal processing tools applied to power quality analysis: IEEE Transactions on Power Delivery, **14**(2), 561-565.

Prada, C., Wu, F., and Fink, M., 1991, The iterative time reversal mirror: A solution to self-focusing in the pulse echo mode: The Journal of the Acoustical Society of America, **90**(2), 1119-1129.

Rousset, D., Sénéchal, G., and Gaffet, S., 2009, GPR investigations in galleries buried inside a karstified limestone formation: EGU General Assembly Conference Abstracts, 10562.

Santos, V. R. N., and Teixeira, F. L., 2017, Application of time-reversal-based processing techniques to enhance detection of GPR targets: Journal of Applied Geophysics, **146**, 80-94.

Taflove, A., and Hagness, S., Computational Electromagnetics, The Finite Difference Time-Domain Method: Artech House, Inc.

Tao, M., Chen, X., Cheng, Q., and Binley, A., 2022, Evaluating the joint use of GPR and ERT on mapping shallow subsurface features of karst critical zone in southwest China: Vadose Zone Journal, **21**(1).

Thomas, S. B., and Roy, L. P., 2021, Impact of GPR antenna height in estimating coal layer thickness using spatial smoothing techniques: IET Science, Measurement and Technology, **14**(10), 906-912.

Torrence, C., and Compo, G. P., 1998, A practical guide to wavelet analysis: Bulletin of the American Meteorological Society, **79**(1), 61-78.

Tosti, F., and Slob, E., 2015, Determination, by using GPR, of the volumetric water content in structures, substructures, foundations and soil: Civil Engineering Applications of Ground Penetrating Radar, 163-194, Springer, Cham.

Wang, Y., 2006, Inverse Q-filter for seismic resolution enhancement: Geophysics, **71**(3), V51-V60.

Yavuz, M. E., Fouda, A. E., and Teixeira, F. L., 2014, GPR signal enhancement using sliding-window space-frequency matrices: Progress In Electromagnetics Research, **145**, 1-10.

Yavuz, M. E., and Teixeira, F. L., 2006, Full time-domain DORT for ultrawideband electromagnetic fields in dispersive, random inhomogeneous media: IEEE Transactions on Antennas and Propagation, **54**(8), 2305-2315.

Yavuz, M. E., and Teixeira, F. L., 2009, Ultrawideband microwave sensing and imaging using time-reversal techniques: A review: Remote Sensing, **1**(3), 466-495.

Zhang, L., Ling, T., Yu, B., Huang, F., and Zhang, S., 2021, Intensive interferences processing for GPR signal based on the wavelet transform and FK filtering: Journal of Applied Geophysics, **186**, 104273.

Appendix

Explanations about compensated time reversal theory (Abduljabbar et al., 2017):

The Morlet wavelet (Morlet et al., 1982; Braga and Moraes, 2013) has been selected to analyze the propagating wave in attenuating and dispersive media according to the aforementioned methods. Torrence and Compo (1998) gave the following definition of a wavelet in a time domain:

$$\Psi_0[n] = \frac{1}{\sqrt[4]{\pi}} e^{Jf_{cm}n\Delta t} e^{-\frac{(n\Delta t)^2}{2}} \quad \text{(A. 1)}$$

where f_{cm} is the central frequency of mother wavelet. n is the time index. It is the time step in seconds. J is the imaginary unit. It is the time step in minutes. The expression for $\Psi_0[n]$ in a scaled-frequency domain is:

$$\Psi_0(a_j\omega_k) = \frac{1}{\sqrt[4]{\pi}} e^{-\frac{(a_J\omega_k - f_{cm})^2}{2}} \quad \text{(A. 2)}$$

where a_j is the dimensionless scaling as $a_j = a_0 2^{j\Delta_j}$ for $j = 01, \cdots, J-1$. a_0 is the smallest scale and J is the largest scale: $J = \left[\frac{1}{\Delta_j}\log_2\left(\frac{N\Delta t}{a_0}\right)\right]$. N is the number of samples in the time domain signal, k is the frequency index and ω_k is the angular frequency given by (Torrence and Compo, 1998):

$$\omega_k = \begin{cases} 0 & k = 1 \\ \frac{2\pi k}{N\Delta t} & 1 < k \leq \frac{N}{2} + 1 \\ -\frac{2\pi k}{N\Delta t} & \frac{N}{2} + 1 < k \leq N \end{cases} \quad \text{for k= 1, 2,…,N and } \Delta j = \Delta t = 0.025$$

A wavelet should typically be accepted, and this is possible when (Farge, 1992):

$$\lim_{N\to\infty} \sum_{n=-N}^{N} \Psi_0[n] = 0 \quad \text{and} \quad \Psi_0(a_j\omega_k) = \begin{cases} \frac{1}{\sqrt[4]{\pi}} e^{-\frac{(a_J\omega_k - f_{cm})^2}{2}} & \omega_k > 0 \\ 0 & \omega_k \leq 0 \end{cases} \quad \text{(A. 3)}$$

The CWT of the observed signal x[n] is represented as the first step in the compensation procedure:

$$X[n, a_j] = \sum_{k=1}^{N} \left(\sum_{i=1}^{N} x[i]\, e^{-J\frac{2\pi}{N}ik} Y^*(a_j w_k)\right) e^{J\frac{2\pi}{N}nk} \quad \text{(A. 4)}$$

The attenuation must first be determined in order to produce an inverse filter. The inverse filter is then applied to $X[n,a_j]$ in the wavelet domain to correct for attenuation. According to Taflove and Hagness (2005), the Maxwell equations' solution for a plane wave propagating in a dispersive medium is:

$$E[n] = e^{J2\pi f.n\Delta t} e^{-J2\pi f\sqrt{\varepsilon\mu}d[n]} \quad \text{(A. 5)}$$

That can be written as:

$$E[n] = e^{J2\pi f.n\Delta t} e^{-J2\pi f\sqrt{\varepsilon_r}\frac{d[n]}{c}}$$
$$= e^{J2\pi f.n\Delta t} e^{-J2\pi f\Re[\sqrt{\varepsilon_r}]\frac{d[n]}{c}} e^{2\pi f\Im[\sqrt{\varepsilon_r}]\frac{d[n]}{c}} \quad \text{(A. 6)}$$
$$\triangleq e^{J2\pi f.n\Delta t}.\Theta.\Gamma$$

where d[n] is the distance between the excitation and the observation, f is the frequency, J is the imaginary unit, $\mu = \mu_0\mu_r$ is the magnetic permeability of the medium, μ_0 is the free space magnetic permeability and μ_r is the relative magnetic permeability of the dispersive medium. $\varepsilon = \varepsilon_0\varepsilon_r$ is the permittivity of the medium, ε_0 is the free space permittivity, ε_r is

the complex relative permittivity of medium. $C = \frac{1}{\sqrt{\varepsilon_0 \mu_0}}$ is the speed of light in the vacuum, $\Re[\sqrt{\varepsilon_r}]$ and $\Im[\sqrt{\varepsilon_r}]$ are the real and the imaginary parts of $\sqrt{\varepsilon_r}$. Γ is the attenuation and Θ is the phase shift defined as:

$$\Gamma[n,f] = e^{2\pi f \Im[\sqrt{\varepsilon_r}]\frac{d[n]}{C}} \quad \text{and} \quad \Theta[n,f] = e^{-J2\pi f \Re[\sqrt{\varepsilon_r}]\frac{d[n]}{C}} \tag{A. 7}$$

The inverse filter extracted from the above equation is:

$$H[n, a_j] = \frac{1}{\Theta[n,a_j].\Gamma[n,a_j]} = e^{J2\pi\frac{f_c}{a_j}\Re[\sqrt{\varepsilon_r}]\frac{d[n]}{C}} e^{-2\pi\frac{f_c}{a_j}\Im[\sqrt{\varepsilon_r}]\frac{d[n]}{C}} \tag{A. 8}$$

where a_j is a scaling factor which controls the actual frequency and f_c is the central frequency of $x[n]$, and H should be stabilized (Wang, 2006) as:

$$H_s[n, a_j] = \frac{\Gamma[n, a_j]}{\Gamma[n, a_j]^2 + T}.\frac{1}{\Theta[n, a_j]} \tag{A. 9}$$

The stabilization factor, shown by the symbol Td, is constant across all simulations. The stabilized compensated wave $Y[n, a_j]$ would be:

$$Y[n, a_j] = X[n, a_j]H_s[n, a_j] \tag{A. 10}$$

Lastly, by applying the inverse continuous wavelet transform (ICWT) to $Y[n, a_j]$, the compensated signal will be (Torrence and Compo, 1998):

$$X_c[n] = \frac{1}{C_\delta}\sum_{j=1}^{J}\frac{\Re[Y[n, a_j]]}{\sqrt{a_j}} \tag{A. 11}$$

where $C_\delta = \sum_{j=1}^{J}\frac{\Re[X_\delta[a_j]]}{\sqrt{a_j}}$. For the Morlet wavelet, the CWT of a delta function is calculated as:

$X_\delta[a_j] = \frac{1}{N}\sum_{k=1}^{N}\Psi^*(a_j\omega_k)$.